



Correlation Between the Microstructural Defects and Residual Stress in a Single Crystal Nickel-Based Superalloy During Different Creep Stages

Fangjie Mo^{1,3} · Erdong Wu² · Changsheng Zhang¹ · Hong Wang¹ · Zhengye Zhong¹ · Jian Zhang² · Bo Chen¹ · Michael Hofmann⁴ · Weimin Gan⁵ · Guangai Sun¹

Received: 11 October 2017 / Accepted: 31 January 2018 / Published online: 19 March 2018
© The Korean Institute of Metals and Materials 2018

Abstract

The present work attempts to reveal the correlation between the microstructural defects and residual stress in the single crystal nickel-based superalloy, both of which play the significant role on properties and performance. Neutron diffraction was employed to investigate the microstructural defects and residual stresses in a single crystal (SC) nickel-based superalloy, which was subjected to creeping under 220 MPa and 1000 °C for different times. The measured superlattice and fundamental lattice reflections confirm that the mismatch and tetragonal distortions with $c/a > 1$ exist in the SC superalloy. At the initially unstrained state, there exists the angular distortion between γ and γ' phases with small triaxial compressive stresses, ensuring the structural stability of the superalloy. After creeping, the tetragonal distortion for the γ phase is larger than that for the γ' phase. With increasing the creeping time, the mismatch between γ and γ' phases increases to the maximum, then decreases gradually and finally remains unchanged. The macroscopic residual stress shows a similar behavior with the mismatch, indicating the correlation between them. Based on the model of shear and dislocations, the evolution of microstructural defects and residual stress are reasonably explained. The effect of shear is dominant at the primary creep stage, which greatly enlarges the mismatch and the residual stress. The dislocations weaken the effect of shear for the further creep stage, resulting in the decrease of the mismatch and relaxation of the residual stress. Those findings add some helpful understanding into the microstructure–performance relationship in the SC nickel-based superalloy, which might provide the insight to materials design and applications.

Keywords Superalloy · Creep · Microstructure · Residual stress · Neutron diffraction · Tension

1 Introduction

Due to their excellent high temperature antioxidant property and mechanical properties, single crystal (SC) nickel-based superalloys are widely used as turbine blade materials in

aircraft engines [1]. To a great extent, the perfect properties are owing to the special microstructure with the *fcc* γ -matrix hardened by the cubic-like $L1_2$ γ' -precipitates. Such kind of microstructure is usually controlled through the heat

✉ Guangai Sun
guangaisun_80@163.com
Michael Hofmann
michael.hofmann@frm2.tum.de
Weimin Gan
weimin.gan@hzg.de

¹ Key Laboratory for Neutron Physics of Chinese Academy of Engineering Physics, Institute of Nuclear Physics and Chemistry, Mianyang 621999, China

² Shenyang National Laboratory for Materials Science, Institute of Metal Research, Shenyang 110016, China

³ Shanghai EBIT Lab, Key Laboratory of Nuclear Physics and Ion-beam Application, Institute of Modern Physics, Department of Nuclear Science and Technology, Fudan University, Shanghai 200433, China

⁴ Forschungsneutronenquelle Heinz Maier-Leibnitz (FRM II), Technische Universität München, 85747 Garching, Germany

⁵ German Engineering Materials Science Centre at MLZ, Helmholtz-Centre Geesthacht, 85747 Garching, Germany

treatment and involves obvious evolution in service. During the heat treatment or in service, some microstructural defects occur in the nickel-based superalloys, such as the dislocation networks, mismatch, lattice misorientation, lattice distortion, shear and so on [2–5]. Those microstructural defects play the important role on the mechanical behavior of superalloys. Therefore, an adequate understanding of the mechanical performance (for example, creep behavior) needs the investigation of the microstructural defects.

At different creep stages, the microstructural defects of SC nickel-based superalloys show distinct features. For instance, at the middle stage of creep, the special hexagonal dislocation networks form and always show peculiar consequences like relaxing the residual stress in superalloys [5–7]. However, before the completion of dislocation networks, the shear of the superalloys can't be ignored [8]. The shear of the phases affects the value of mismatch and lattice distortions with *cla*. In addition, the mismatch and distortions, which have important effect on microstructural stability of the superalloys, vary with the element diffusion [2, 9]. Due to the element diffusion, the cubic-like γ' phase keeps coarsening and lengthens in the direction perpendicular to extra tensile stress [10–12]. However, the macroscopic response such as internal residual stress and its interaction with the microstructural defects have not been addressed adequately in nickel-based superalloys.

The residual stress is an important parameter to estimate the properties of SC nickel-based superalloys [13]. It has been known that the residual stress in superalloys could be indirectly affected by the adjustment of the microstructure [7, 14, 15]. For example, the γ' phase rafting structure including the raft length, thickness and orientation with microstructural defects, correlates possibly with the distribution of residual stresses [12, 16, 17]. Actually, the experimental set-up of measuring residual stress for SC superalloys is more complicated than that for polycrystalline superalloys [18]. Therefore, most investigations for residual stress in superalloys have been concentrated on polycrystalline materials, while the study about the residual stress of SC superalloys was rare [19]. Meanwhile, the relationship between microstructure and residual stresses in SC superalloys has not been clearly discussed.

There are several methods to study the microstructure and residual stresses, among which X ray diffraction (XRD) and neutron diffraction are commonly used as the non-destructive ones to measure residual stresses. Compared with XRD, neutron diffraction is better to distinguish the strong overlaps of γ and γ' superlattice reflections [20]. Moreover, neutron wavelength is always adjustable to control the diffraction angle and minimize the experimental errors. In addition, the penetrability of neutron diffraction (cm) is much stronger than XRD (μm). Therefore, the three dimensional microstructural data inside the bulk materials can be directly obtained by neutron diffraction rather than XRD [21].

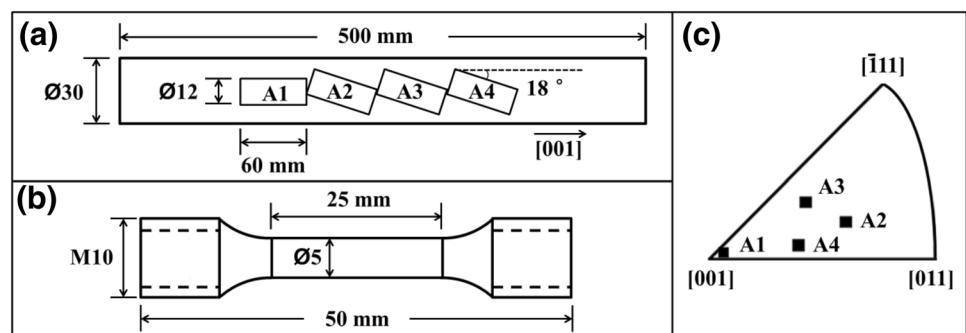
Therefore, the present work investigates the evolution of microstructure and the residual stresses through the combined advantage of neutron diffraction aforementioned above. Both the microstructural defects including the lattice mismatch and the residual stress tensor have been quantitatively obtained in the single crystal nickel-based superalloy. The evolution of the rafting structure has been measured by transmission electron microscopy (TEM). Those data add some helpful understanding into the microstructure-performance relationship in the SC nickel-based superalloy, which might provide the insight to materials design and applications.

2 Experiments

2.1 Materials

The materials used in the experiment were DD10 SC nickel-based superalloys. Their nominal chemical compositions (wt%) were as follows: 13.0Cr, 4.0Co, 5.3Al, 4.1Ti, 3.1Ta, 3.9 W, 2.3Mo, with the addition of minor C and B, and the balance Ni, developed by the Institute of Metal Research, Chinese Academy of Science. The maternal rod of cylindrical samples was 500 mm long and 30 mm in diameter, which was grown along the [001] direction by unidirectional solidification. To reduce the differences of compositions or other states between the samples, each sample with 60 mm in length and 12 mm in diameter was cut from the middle region in the

Fig. 1 **a** The preliminary sketch of the cylindrical samples cut from a maternal rod grown along [001] direction (denoted as A1, A2, A3, A4), **b** the tensile specimen dimension, **c** orientations of samples in the stereographic unit triangle



maternal rod. Hence, the samples were machined into the tensile specimen dimension exhibited in Fig. 1b.

As shown in Fig. 1a, the first sample denoted as A1 was cut parallel to the [001] direction, used as the initial sample. To bring in the microstructural defects strongly, the other three samples were cut with 18° deviation from [001] direction, which were subjected to different heat treatment (denoted as A2, A3, A4 respectively). Figure 1c illustrates schematically the orientations of A1, A2, A3 and A4 samples in the stereographic unit triangle. The A1 sample was parallel well with the [001] direction from which the sample orientation had only 3° deviation. The A2 sample had the largest angle deviation of 22°, while A4 display the small angle deviation of 17°. Though A2, A3 and A4 should have similar orientation, owing to the machining process and experimental errors, the orientations of them show a small divergence. Therefore, we assumed the states of the three samples were the same. Those samples were standard heat treated at 1250 °C/3 h/air cooling (AC)+1100 °C/5 h/AC+870 °C/24 h/AC.

Hence, A1 was heated to 1000 °C for 1.5 h and then kept for 1 h, following by AC, which was the annealed control sample. A2, A3 and A4 were heated to 1000 °C for 1.5 h, and then they were creep tested under 220 MPa and 1000 °C, respectively for 1.5, 8 and 24 h, following by AC. As shown in the tensile creep curve of Fig. 2, the creep time 0, 1.5, 8 and 24 h were chosen to correspond with the conditions of different creep stages, which were respectively the initially unstrained stage, first creep stage, second creep stage and third creep stage. The microstructure of the four samples was measured by TEM.

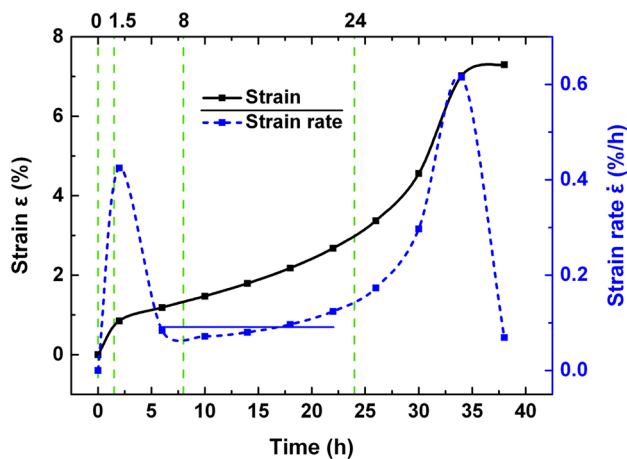


Fig. 2 The tensile creep curve of DD10 superalloy under 220 MPa and 1000 °C along [001] orientation with 18° deviation. The solid line stands for strain and the dot line stands for strain rate. The horizontal solid line stands for the plateau of strain rate. The vertical dash lines stand respectively for the creep time 0, 1.5, 8, and 24 h corresponding with the samples A1–A4

2.2 Neutron Diffraction

The neutron diffraction measurements were carried out on the strain scanning instrument STRESS - SPEC at FRM II in the Technical University of Munich in Germany [22]. As shown in Fig. 3, the rotational relationship of the sample step-up is clear, where φ and χ represents respectively the sample's rotation and tilting, whilst Ω represents the sample table's rotation. The measured reflections corresponded well with the rotational relationship of the samples. In order to minimize the measuring errors, the scattering angle 2θ was chosen at approximately 90° defining a cubic gauge volume $2 \times 2 \times 2 \text{ mm}^3$. Because of the variety of the experimental reflections, the incident wavelength λ was changed between 1.109, 1.221 and 1.737 Å using the monochromator of Ge (511). The resolution of the instrument was determined to be 0.002° and $\Delta d/d$ was about $\pm 2 \times 10^{-4}$ at the scattering angle.

The measuring points were all chosen at the center of the samples and multiple crystal planes were involved as follows: {003}, {004}, {022}, {033}, and {331}. The {003} and {033} were chosen as superlattice reflections, while the {004}, {022} and {331} were chosen as fundamental reflections. In most systems of superalloys, the lattice parameters of γ and γ' phases are too close to be distinguished in the diffraction profiles. Therefore, to derive the d -spacing of the reflections of γ and γ' phases, the different fitting strategy was respectively used for the fundamental and superlattice reflections. The single-peak fitting was used for {003} and {033} reflections, while for {004}, {022} and {331} the dual-peak fitting was used.

However, some restrains should be followed for the dual-peaks fitting [2]: (1) the Gaussian function was used as the fitting function with the assumption of a symmetric profile, (2)

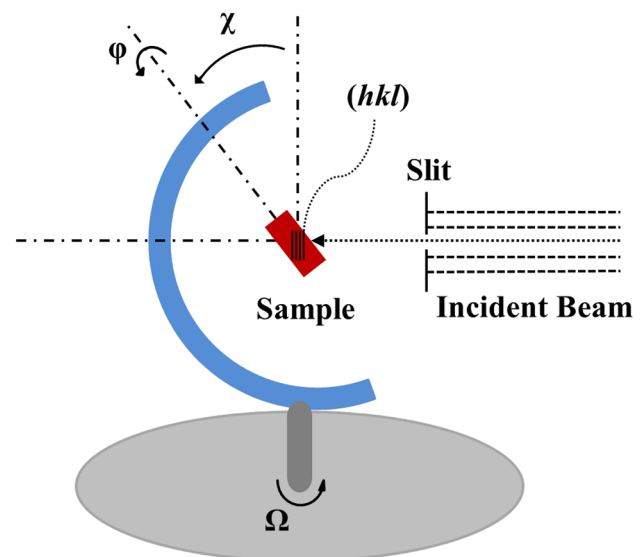


Fig. 3 The schematic diagram of the geometry of the experimental set-up

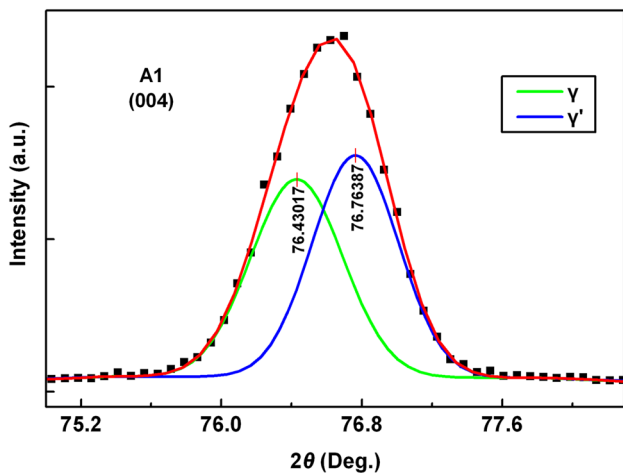


Fig. 4 The dual-peak fitting of the (004) fundamental reflection for the unstrained sample A1. The raw data are the discrete square symbols and the other lines are results of fitting profiles

the intensity of two phases was fixed on the assumption that the volume fraction of the γ' phase was 60% and the balance γ phase, (3) the peak positions was fixed well between the fundamental and superlattice reflections to ensure the fitting results much valid. Figure 4 shows one of the peak profiles for the (004) reflection of sample A1. Through the strategy of dual-peak fitting, the results were more reliable than those carried out by only using single-peak fitting of the fundamental reflections. Hence, the d -spacing of the planes could be derived from different orientations in the lattice. For example, the d -spacing of {004} planes could be derived from (004), (040) and (400) which shared the same diffraction angle. Through the peak fitting, the positions of the peaks could be determined and each lattice parameter could be calculated by Bragg equation.

The errors derived from the deviations of the measurements could judge the accuracy of the measurements. Therefore, the uncertainty of experiments possibly influenced the analysis of the small difference in lattice parameters. For example, the uncertainty of fitting peak position was about $\pm 5 \times 10^{-4}^\circ$. The fluctuation of room temperature also contributed to the change in 2θ of $\sim \pm 5 \times 10^{-4}^\circ\text{C}$ [3]. Thus the associated error in d -spacing mainly derived from the calculated error of peak fitting, fluctuation of room temperature and resolution of the instrument. Moreover, at least two different reflections were measured for each type of plane. Therefore, it is fair to assume that the error of d -spacing was $\pm 1.7 \times 10^{-4} \text{ \AA}$ in the γ phase and $\pm 2.5 \times 10^{-4} \text{ \AA}$ in the γ' phase. Hence, the error bars were calculated and showed in the following figures.

Table 1 The elastic coefficients of γ and γ' phases at room temperature

	C_{11} (GPa)	C_{12} (GPa)	C_{44} (GPa)
γ phase	220	120	130
γ' phase	170	90	100
Macro	200	100	110

2.3 Residual Stress Analysis

The type I and average type II stresses could be calculated by the peak shift [23]. Hence, the stress could be carried out using the stiffness C of the material. Considering the SC material with strong anisotropy, the stiffness C always varied between different orientations. In the present work, the stiffness C of {331} was chosen to calculate the stresses [13]. The elastic strain was calculated by the equation:

$$\varepsilon = \frac{d_{\varphi\chi} - d_{0,\varphi\chi}}{d_{0,\varphi\chi}} = \varepsilon_{11} \cos^2 \varphi \cos^2 \chi + \varepsilon_{22} \sin^2 \varphi \cos^2 \chi + \varepsilon_{33} \sin^2 \chi + \varepsilon_{12} \sin 2\varphi \cos^2 \chi + \varepsilon_{13} \cos \varphi \sin 2\chi + \varepsilon_{23} \sin \varphi \sin 2\chi \quad (1)$$

where $d_{\varphi\chi}$ is the d -spacing at the rotational angle of φ and χ , $d_{0,\varphi\chi}$ is the stress free spacing, ε_{ij} is strain tensor component in sample coordinate system [24]. However, when d_0 was set as a reasonable invariant, the d_0 was not necessary to be measured with the sufficient value [3]. In this work, the average lattice parameters of each state of {331} in γ or γ' phase were used as the d_0 . The analysis of the data was self-consistent. In order to ensure the accuracy of analysis, 10 or 11 values of d -spacing were used.

Based on Hooke's law, the stress tensor components σ_{ij} were simplified by the following expression:

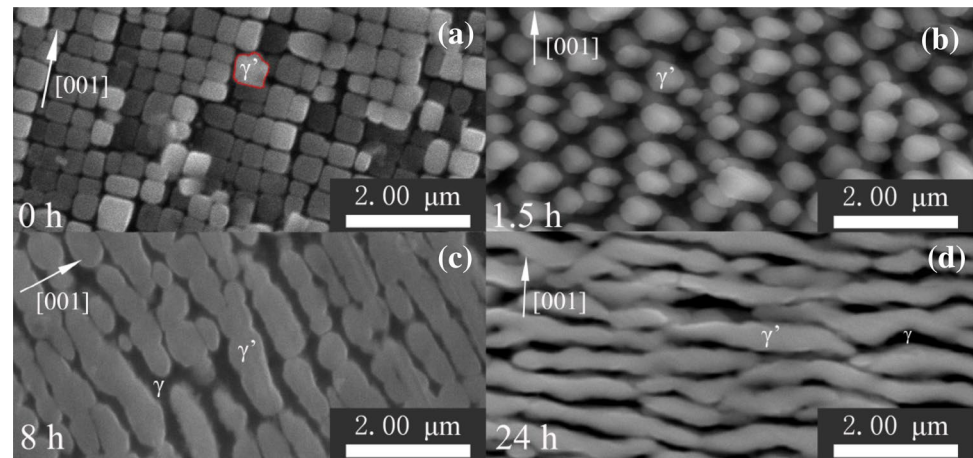
$$\sigma_{ij} = C_{ijkl} \varepsilon_{kl} = \frac{E_{hkl}}{1 + \nu_{hkl}} \left(\varepsilon_{ij} + \frac{\nu_{hkl}}{1 - 2\nu_{hkl}} \varepsilon_{kk} \delta_{ij} \right) \quad (2)$$

where E_{hkl} is Young's modulus of (hkl) , ν_{hkl} is the Poisson's ratio of (hkl) , δ_{ij} is the Kronecker delta-function. In this study, the elastic coefficients in the $\langle 331 \rangle$ orientation at room temperature were taken from the Ref. [10, 25] as shown in Table 1. Though the values were not really accurate, it's reliable that the chemical compositions and the heat treatments of the superalloy were close.

In addition, the equivalent von Mises stress σ_{Mises} was used to evaluate the magnitude of local stresses:

$$\sigma_{Mises} = \sqrt{\frac{1}{2} \left[(\sigma_{11} - \sigma_{22})^2 + (\sigma_{22} - \sigma_{33})^2 + (\sigma_{33} - \sigma_{11})^2 + 6(\sigma_{12}^2 + \sigma_{23}^2 + \sigma_{31}^2) \right]} \quad (3)$$

Fig. 5 The microstructure of the samples for different creep times measured by TEM: **a** initially unstrained sample A1, **b** 1.5 h sample A2, **c** 8 h sample A3, **d** 24 h sample A4. The γ and γ' phases are marked in the photos. The arrow stands for the [001] orientation



3 Results and Discussion

3.1 Evolution of the Microstructure

The evolution of the microstructure of γ and γ' phases were measured by TEM, as exhibited in Fig. 5. For different creep stages, the microstructure of γ and γ' phases shows typical features. The initial sample A1 (Fig. 5a) shows the typical microstructure that the regular cubical γ' precipitates align embedding in the γ matrix. The cubical γ' precipitates are $\sim 0.4 \mu\text{m}$ in edge width, whereas the γ channel is $\sim 0.05 \mu\text{m}$ in width.

After creeping for 1.5 h (Fig. 5b), the microstructure of the cubical γ' precipitates doesn't change much except for the dissolution of the edges and corners. It will result in the coarsening of γ' precipitates leading to the structure rafting [10–12]. This phenomenon is reported for the reason of the shear effect, when the dislocation networks are less developed for the primary creep stage [8]. To balance the free energy between the phases, the atoms of the edges and corners of γ' phase successively diffuse [10]. Under the high temperature, γ' phase is relatively stiffer than γ phase. Therefore, the dislocations prefer to propagate in the γ phase [26]. For the nonequilibrium state of the element diffusion, the distortion and the mismatch between γ and γ' phases should increase at this creep stage.

As the creep time elapsing, due to the element diffusion, the rafting structure of γ' phase forms for the time of 8 h (Fig. 5c). The rafting structure is $\sim 0.6 \mu\text{m}$ in width and $\sim 3 \mu\text{m}$ in length, whereas the horizontal γ channel (compared with the [001] orientation) is $\sim 0.2 \mu\text{m}$ in width and parallel channels are gradually eliminated. Apparently, the move of dislocations in γ phase should be impeded by the rafting structure. As a result, the dislocations concentrate more on the interfaces between γ and γ' phases [5]. Hence, the dislocation networks successively form on the interfaces

[5]. At next creep stage, the rafting structure of γ' phase is almost completed for the time of 24 h (Fig. 5d). As shown in Fig. 5d, the parallel γ channels are eliminated, while the length of the rafting structure is $> 4 \mu\text{m}$. At this stage, the dislocations largely generate and concentrate on the interfaces between γ and γ' phases. The hexagonal dislocation networks complete [5].

3.2 Lattice Parameters of γ and γ' Phases

Figure 6 shows the average lattice parameters of the measured reflections as a function of the creep time. Before the creep test, the lattice parameter of γ and γ' phases is respectively ~ 3.585 and $\sim 3.571 \text{ \AA}$. With the increase of creep time, the average lattice parameters of planes largely

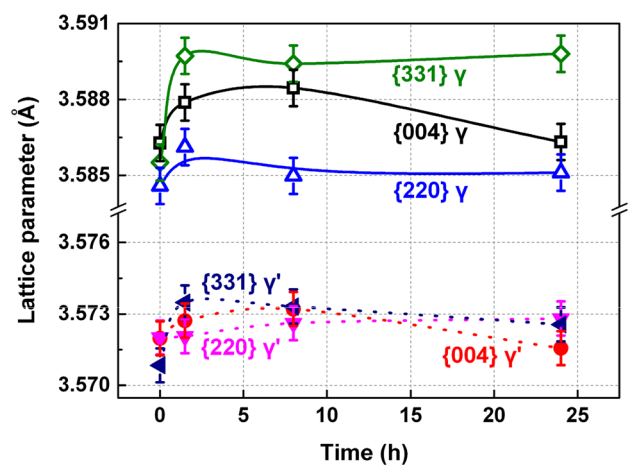


Fig. 6 The average lattice parameters of each family of the planes {004}, {220} and {331} for the time of 0, 1.5, 8 and 24 h (sample A1, A2, A3, A4). The hollow symbols and the solid line stand for γ phase, while the solid symbols and the dot line stand for γ' phase. The errors are discussed in Sect. 2.2

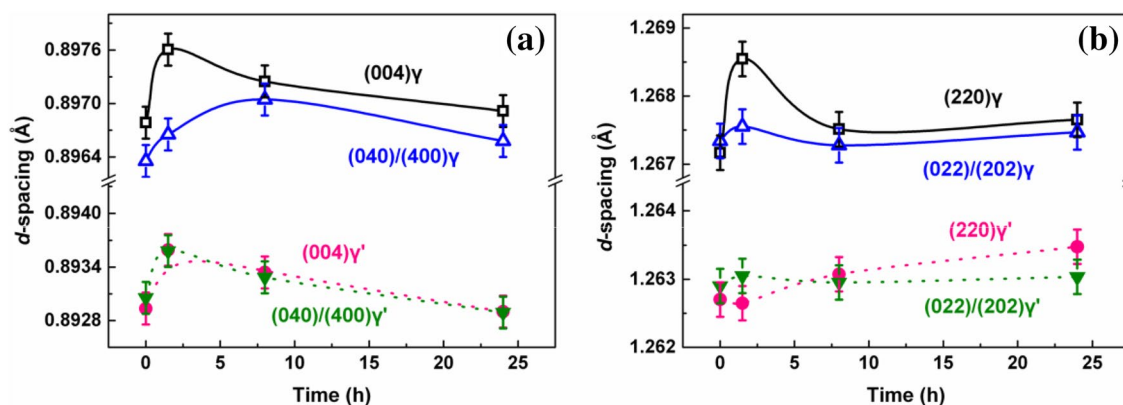


Fig. 7 The d -spacing of each type of planes for the time of 0, 1.5, 8 and 24 h (sample A1, A2, A3, A4): **a** d -spacing of (004) and (040)/(400), **b** d -spacing of (220) and (022)/(202). The hollow symbols and

the solid line stand for γ phase, while the solid symbols and the dot line stand for γ' phase

increase for the time of 1.5 h and then change slightly. The average parameter of γ phase is around 3.587 Å, while that of γ' phase is approximately 3.573 Å. Therefore, there is the interfacial stress in the coherent phase boundary and the mismatches between the phases behave negative [2].

As can be seen in Fig. 6, the average lattice parameters of sample A1 (0 h) concentrate in a small range. The parameters of γ phase are from 3.5846 to 3.5863 Å, while those of γ' phase are 3.5708–3.5720 Å. It indicates that the distortion in sample A1 is relatively small. In addition, after creeping, the distribution of lattice parameters of γ' phase is concentrated at the value of 3.573 Å, whereas that of the γ phase is comparatively disperse. This phenomenon suggests that the tetragonal distortion for γ phase is more obvious than that for γ' phase.

Figure 7 shows the d -spacing of each type of planes as the function of creep time. In detail, we assume that the results of the reflections, which have the similar deviation with the strain direction, are the same. The lattice planes are divided into two types: (004) is perpendicular to [001] and (040)/(400) are parallel to [001], while (220) is parallel to [001] and (022)/(202) deviate 45° from [001]. The d -spacing of two types are close for each creep stage, except for the d -spacing of (004) and (220) at 1.5 h for γ phase. After creeping for 1.5 h, the d -spacing of (004) and (220) is larger than that of (040)/(400) and (022)/(202) for γ phase, while the d -spacing for γ' phase are close to each other for all the testing time. This phenomenon possibly results from the interaction between shear and dislocations of γ phase [5, 7, 8]. Figure 8 shows the dislocation densities ρ of the samples for different times, which are calculated by the equation [27]:

$$\rho = \frac{\beta^2}{4.35b^2} \quad (4)$$

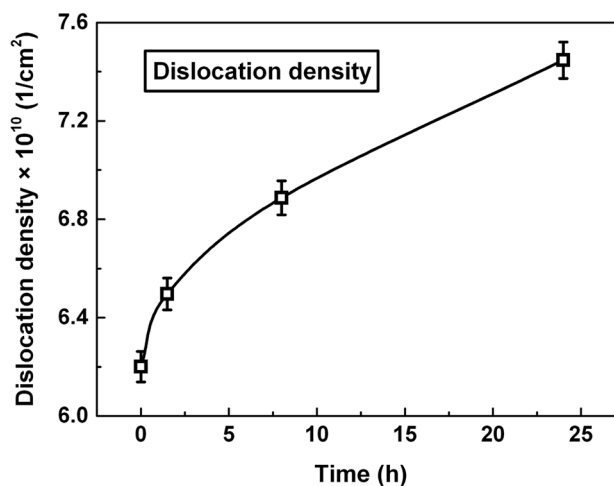


Fig. 8 The dislocation density for the time of 0, 1.5, 8 and 24 h (sample A1, A2, A3, A4)

where β is integral breadth and b is the value of the Burgers vector. The values of β are carried out by the average integral breadth of {004} and {220} reflections and the value of b is 2.53×10^{-8} cm. The dislocation density in the superalloy increases as the creep time growing. With the dislocations generate, the microstructure of dislocations gradually evolves [5]. In the primary creep stage, the main dislocations are $a/2$ [101] and $a/2$ [011] located at the γ and γ' interface. Hence, some $a/2$ [101] and $a/2$ [011] dislocations react to form $a/2$ [110] secondary dislocations [4, 5]. However, for the creep stage of 1.5 h, the dislocations are not largely generated and the hexagonal dislocation networks are absent. Thus, the effect of {111} <110> shear dominates the deformation [28, 29]. As a result, the d -spacing of (220) and (004) shows relatively larger values due to the occurrence of the

shear in γ phase [30]. However, after the creep stage of 1.5 h, the $a/2 \langle 110 \rangle$ dislocations largely generate and the hexagonal dislocation networks gradually form to accommodate the effect of the small shear [8]. Therefore, the d -spacing in γ phase generally decrease.

3.3 Lattice Distortions and Mismatch

The average mismatches and the lattice distortions with c/a in the γ and γ' phases are exhibited in Fig. 9, where c is the average lattice parameter of (004) and a is the average lattice parameter of (040)/(400). Actually, the condition of the lattice distortion reflects the evolution of lattice shear. The lattice distortion with c/a for the γ phase is larger than that for the γ' phase for all the test time. Before creep test, the γ phase shows the tetragonal distortions with $c/a > 1$, while the γ' phase shows an opposite result with $c/a < 1$. This result suggests that between the γ and γ' phases, some angular distortions exist as the schematic diagram shown in Fig. 10. The angular distortions, which proceed from the growing process

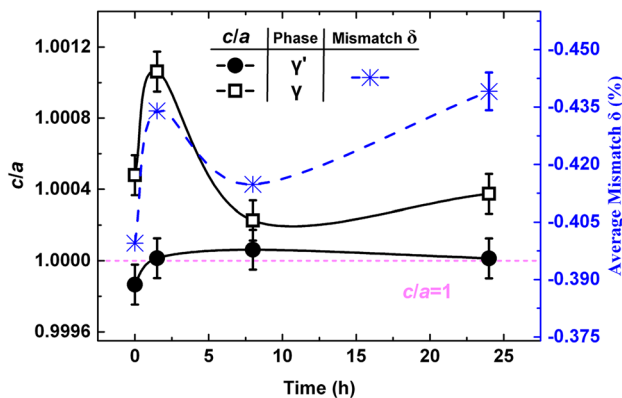


Fig. 9 The value of c/a of the unit cells of γ and γ' phases and the average mismatches for different states. The horizontal dot line stands for $c/a=1$. The hollow and solid symbols respectively stands for γ phase and γ' phase, while the star symbols and dash line stand for mismatch

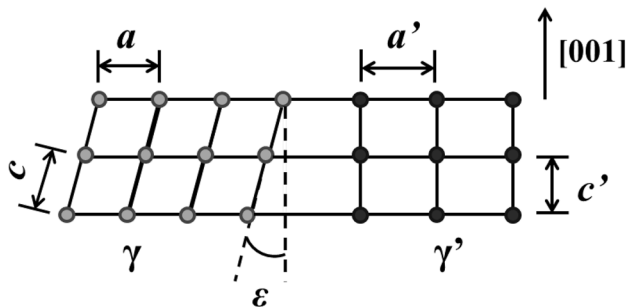


Fig. 10 The schematic diagram of the local lattice angular distortion between γ and γ' phases

and heat treatments, reveal the misorientation between the γ and γ' phases. However, after creep test for 1.5 h, the γ phase shows the tetragonal distortions with $c/a > 1$, while that for the γ' phase is ~ 1 . This phenomenon, as discussed before, results from the lattice shear in γ phase and absence of the complete dislocation networks in the primary creep period [31, 32]. Then the tetragonal distortions with c/a in γ phase sharply decrease for the creep time of 8 h. It results from the forming of dislocation networks which decline the effect of lattice shear [3]. In the further creep period of 24 h, the distortion changes little in the γ phase. However, the γ' phase almost doesn't show the obviously tetragonal distortion for the entire creep test. It indicates the microstructural defects in γ' phase less develop.

The mismatch δ between γ and γ' phases can be obtained by the expression [33]:

$$\delta = \frac{2(a_{\gamma'} - a_{\gamma})}{a_{\gamma'} + a_{\gamma}} \quad (5)$$

where $a_{\gamma'}$ and a_{γ} are the lattice parameters of γ and γ' phases, respectively. As illustrated in Fig. 9, the negative mismatch confirms the fact that γ phase endures the compressive stress and γ' phase endures the tensile stress in the superalloy. The mismatch increases sharply after creep test for 1.5 h. Hence, the mismatch decreases for the creep time of 8 h. This result corresponds with the change of the tetragonal distortions in the γ and γ' phases. For the creep test time of 24 h, the forming of the dislocation networks increases the mismatch between the γ and γ' phases [5].

The mismatches of different types (type (004) and type (040)/(400), type (220) and type (022)/(202)) of lattice planes are given in Fig. 11. For the effect of creep test, the mismatch increases for the first creep period of 1.5 h.

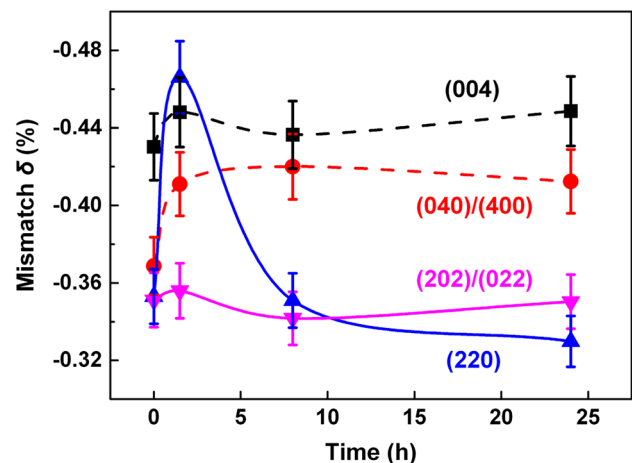


Fig. 11 The mismatches for γ and γ' phases of different types of lattice planes for the time of 0, 1.5, 8 and 24 h (sample A1, A2, A3, A4): {004} and {220} are shown. The dash line stands for {004} and the solid line stands for {220}

Table 2 The strain and stress tensor of the γ and γ' phases in SC coordinate system of A1, A2, A3, and A4 samples (0, 1.5, 8, 24 h)

Sample	A1 (0)	A2 (1.5 h)	A3 (8 h)	A4 (24 h)
<i>Strain tensor ($\times 10^{-4}$)</i>				
γ	$\begin{bmatrix} -0.5 & 1.6 & -3.9 \\ 1.6 & -3.9 & 0.7 \\ -3.9 & 0.7 & 2.4 \end{bmatrix}$	$\begin{bmatrix} -6.0 & 4.5 & 1.6 \\ 4.5 & -2.0 & -3.2 \\ 1.6 & -3.2 & 7.0 \end{bmatrix}$	$\begin{bmatrix} -1.9 & -6.2 & 3.5 \\ -6.2 & -3.7 & 4.2 \\ 3.5 & 4.2 & 5.7 \end{bmatrix}$	$\begin{bmatrix} -5.9 & -3.3 & 1.6 \\ -3.3 & -7.9 & 0.7 \\ 1.6 & 0.7 & 7.7 \end{bmatrix}$
γ'	$\begin{bmatrix} 3.0 & 6.7 & -4.6 \\ 6.7 & -5.0 & -5.8 \\ -4.6 & -5.8 & 0.9 \end{bmatrix}$	$\begin{bmatrix} -6.2 & 3.0 & 4.6 \\ 3.0 & -3.3 & -3.0 \\ 4.6 & -3.0 & 6.8 \end{bmatrix}$	$\begin{bmatrix} -3.0 & -3.8 & 1.7 \\ -3.8 & -1.6 & 4.1 \\ 1.7 & 4.1 & 3.0 \end{bmatrix}$	$\begin{bmatrix} -0.7 & -4.1 & 0 \\ -4.1 & -3.3 & -0.3 \\ 0 & -0.3 & 3.2 \end{bmatrix}$
<i>Stress tensor (MPa)</i>				
γ	$\begin{bmatrix} -30 & 40 & -101 \\ 40 & -63 & 18 \\ -101 & 18 & -1 \end{bmatrix}$	$\begin{bmatrix} -71 & 117 & 42 \\ 117 & -32 & -84 \\ 42 & -84 & 59 \end{bmatrix}$	$\begin{bmatrix} -18 & -162 & 92 \\ -162 & -36 & 108 \\ 92 & 108 & 58 \end{bmatrix}$	$\begin{bmatrix} -132 & -86 & 40 \\ -86 & -152 & 18 \\ 40 & 18 & 4 \end{bmatrix}$
γ'	$\begin{bmatrix} 14 & 134 & -92 \\ 134 & -49 & -115 \\ -92 & -115 & -2 \end{bmatrix}$	$\begin{bmatrix} -73 & 59 & 92 \\ 59 & -51 & -60 \\ 92 & -60 & 30 \end{bmatrix}$	$\begin{bmatrix} -45 & -76 & 34 \\ -76 & -33 & 82 \\ 34 & 82 & -1 \end{bmatrix}$	$\begin{bmatrix} -12 & -82 & 0 \\ -82 & -33 & -6 \\ 0 & -6 & 19 \end{bmatrix}$

The planes of (004) and (040)/(400) show the close mismatches, while the mismatch of (220) shows a relatively large increase. After 1.5 h for latter creep periods, the mismatches of {004} and (202)/(022) don't show much change, whereas the mismatch of (220) falls sharply. These results indicate that during the first creep period, the forming of shear increases the mismatch of (220), while after 1.5 h, the primary dislocations $a/2 \langle 110 \rangle$ are generated to accommodate the effect of shear. The large changes of the mismatch of (220) also reflect the disproportionation of the γ and γ' lattice structure [8]. In conjunction with the results of average mismatches in Fig. 9, the decrease of the average mismatch after 1.5 h mainly results from the decline of the (220) mismatch.

3.4 Results of the Residual Stresses

Table 2 exhibits strain and stress tensor in SC coordinate system calculated from the dual-peak fitting of the fundamental reflections {331}. In the initially unstrained sample A1, the principal strain tensor components $\epsilon_{11}, \epsilon_{22}, \epsilon_{33}$ are small and stress tensor components $\sigma_{11}, \sigma_{22}, \sigma_{33}$ mostly show negative values. This phenomenon suggests that after the solution and aging treatments, the sample endures small triaxial compressive stresses. The stresses possibly proceed from the effect of the limited growing space during unidirectional solidification. However, in the creep samples, the principal strain and stress tensor components correspond well with the actual unidirectional tensile situation that $\epsilon_{11}, \epsilon_{22}/\sigma_{11}, \sigma_{22}$ are negative and $\epsilon_{33}/\sigma_{33}$ are positive [34]. Compared with other creep samples, the principal strain tensor components $\epsilon_{11}, \epsilon_{22}, \epsilon_{33}$ of sample A2 (1.5 h) show the largest values: $-6.0, -2.0, 7.0 \times 10^{-4}$ for γ phase and $-6.2, -3.3, 6.8 \times 10^{-4}$ for γ' phase. On the contrary, those of sample A3 (8 h) show the small values: $-1.9, -3.7, 5.7 \times 10^{-4}$ for γ phase and $-3.0,$

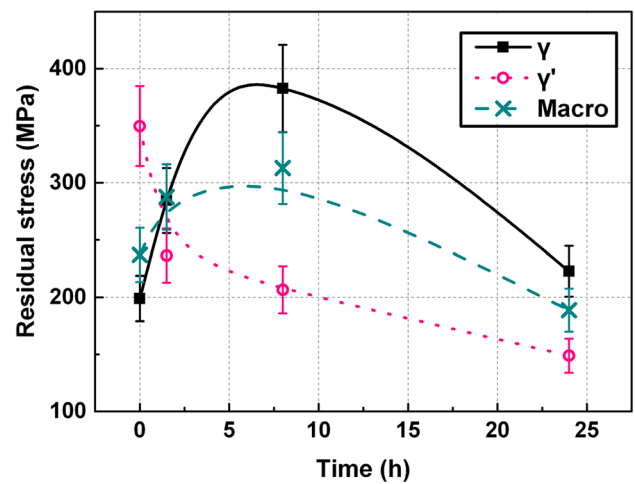


Fig. 12 The von Mises stress evolution of γ and γ' phase stress and macroscopic stress for the time of 0, 1.5, 8 and 24 h (sample A1, A2, A3, A4). The solid line stands for γ phase stress, the dot line stands for γ' phase stress and the dash line stands for macroscopic residual stress

$-1.6, 3.0 \times 10^{-4}$ for γ' phase. The change of the principal strain tensor components coheres well with the evolution of the average mismatches and the tetragonal distortions with c/a . It demonstrates that the effect of distortions is strong at the creep time of 1.5 h and weak for other times.

The von Mises stresses of the γ and γ' phases are calculated from the dual-peak fitting of the fundamental reflections {331}, while the macroscopic von Mises stresses are calculated from the single peak fitting of the {331} as exhibited in Fig. 12. The residual stress for γ' phase decreases, whilst that for γ phase increases for some hours and follows decreasing. The results correspond finely with those calculated by finite element methods (FEM) in Ref. [35]. The increase of residual stresses in γ phase results from the

interaction of shear in γ phase for the creep time of 1.5 h. After creeping of 8 h, the lattice shear is halted in γ phase, whereas the dislocation networks are not completed. Therefore, the residual stress continuously increases. However, the residual stresses in γ' phase decrease during all the testing time. This phenomenon results from the microstructural defects, such as the tetragonal distortions, in γ' phase less develop. The evolution of the macroscopic von Mises stress demonstrates that the residual stress increases for short time and follows stress relaxing. The stress relaxation is due to the dislocation networks, which enhance the incoherency of γ and γ' phases, gradually building up at the interface of γ and γ' phases [5, 7].

From the analysis above, the evolution of microstructural defects (the lattice schematic diagram of the distortion and dislocations in γ phase is shown in Fig. 13) is unfolded and their relationship with residual stresses is discussed: (1) after creeping for 1.5 h, the shear is the dominant microstructural defect in γ phase. It increases the d -spacing, the tetragonal distortions with c/a and the lattice mismatches. Therefore, the residual stress in γ phase increases. (2) At the creep time of 8 h, the shear of γ phase is gradually halted and accommodated by the generating of the primary dislocations like $a/2 \langle 110 \rangle$. Therefore, the tetragonal distortions with c/a and the lattice mismatch decrease. However, the dislocation networks don't complete, so the residual stresses in γ phase still slightly increase. (3) After creeping for 24 h, the effect of shear minimizes, while the dislocation networks build up. As a result, the tetragonal distortions with c/a don't change obviously and the lattice mismatch slightly increases. Therefore, the residual stresses relax.

4 Conclusions

The features of microstructural defects and residual stress were carried out by TEM observation and neutron diffraction measurements of the fundamental and superlattice reflections. We can draw the conclusions from the results as following.

1. The lattice parameters and mismatches show anisotropy. After the 1000 °C/220 MPa creep test, the γ phase shows the tetragonal distortions with $c/a > 1$ at the γ/γ' interfaces for all the testing time, while the values of c/a for γ' phase are ~ 1 . The tendency of the change of average mismatches coheres well with that of the tetragonal distortion with c/a .
2. After creep test, the residual stresses show unidirectional features that the ϵ_{11} , $\epsilon_{22}/\sigma_{11}$, σ_{22} are negative and the $\epsilon_{33}/\sigma_{33}$ are positive. The macroscopic von Mises stress increases for some hours and follows relaxing.

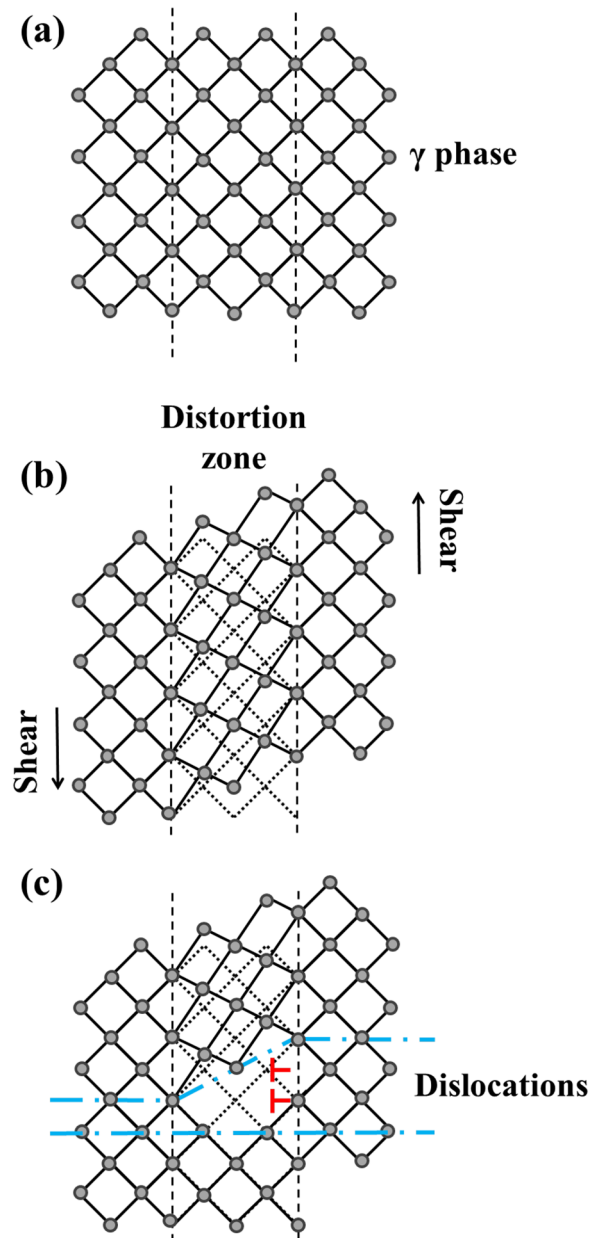


Fig. 13 The lattice schematic diagram of the evolution of the distortion and dislocations for tensile testing in γ phase: **a** for the initially unstrained state, γ phase shows few defects, **b** the shear stress results in the local lattice distortion in γ phase, **c** the dislocations generate and accommodate the effect of distortions

3. The results indicate the evolution of the microstructural defects, such as mismatches and distortions, are relative to the evolution of residual stresses. At the primary creep stage, the macroscopic residual stress and the tetragonal distortion with $c/a > 1$ increase in γ phase. While at latter period, dislocations generate to decrease the mismatch and tetragonal distortion. At the final stage, dislocation networks build up to relax the residual stress and slightly increase the mismatch.

Acknowledgements This work has benefited from the neutron source at FRM II in the Technical University of Munich in Germany. The work is supported by the National Natural Science Foundation of China (51231002 and 51501170), and the Foundation of President of CAEP (2012-1-024).

References

1. G.W. Meetham, M.V.D. Voorde, L. Mishnaevsky, *Appl. Mech. Rev.* **54**, 385 (2001)
2. E. Wu, G. Sun, B. Chen et al., *Acta Mater.* **61**, 2308 (2013)
3. J. Coakley, R.C. Reed, J.L.W. Warwick et al., *Acta Mater.* **60**, 2729 (2012)
4. C.M.F. Rae, R.C. Reed, *Acta Mater.* **55**, 1067 (2007)
5. T. Link, A. Epishin, M. Klaus et al., *Mater. Sci. Eng., A* **405**, 254 (2005)
6. R. Völkl, U. Glatzel, M. Feller-Kniepmeier, *Scr. Metall. Mater.* **31**, 1481 (1994)
7. A. Jacques, F. Diologent, P. Bastie, *Mater. Sci. Eng., A* **387–89**, 944 (2004)
8. C.M.F. Rae, N. Matan, R.C. Reed, *Mater. Sci. Eng., A* **300**, 125 (2001)
9. B. Marty, P. Moretto, P. Gergaud et al., *Acta Mater.* **45**, 791 (1997)
10. L. Müller, U. Glatzel, M. Feller-Kniepmeier, *Acta Metall. Mater.* **40**, 1321 (1992)
11. A. Epishin, T. Link, U. Brückner et al., *Acta Mater.* **49**, 4017 (2001)
12. R.C. Reed, D.C. Cox, C.M.F. Rae, *Mater. Sci. Eng., A* **448**, 88 (2007)
13. P.J. Withers, H.K.D.H. Bhadeshia, *Mater. Sci. Technol.* **17**, 355 (2001)
14. J. Rolph, A. Evans, A. Paradowska et al., *C. R. Phys.* **13**, 307 (2012)
15. B.J. Foss, S. Gray, M.C. Hardy et al., *Acta Mater.* **61**, 2548 (2013)
16. R.C. Reed, D.C. Cox, C.M.F. Rae, *Mater. Sci. Technol.* **23**, 893 (2007)
17. E.I. Galindo-Nava, L.D. Connor, C.M.F. Rae, *Acta Mater.* **98**, 377 (2015)
18. A. Morañais, M. Fèvre, M. François et al., *J. Appl. Crystallogr.* **48**, 1761 (2015)
19. M.E. Kartal, F.P.E. Dunne, A.J. Wilkinson, *Acta Mater.* **60**, 5300 (2012)
20. W. Chen, N. Darowski, I. Zizak et al., *Nucl. Instrum. Meth. B* **246**, 201 (2006)
21. R. Gilles, D. Mukherji, M. Hoelzel et al., *Acta Mater.* **54**, 1307 (2006)
22. M. Hofmann, G.A. Seidl, J. Rebelo-Kornmeier et al., *Phys. B* **385–386**, 1035 (2006)
23. P.J. Withers, *Key Eng. Mater.* **108–110**, 291 (1995)
24. M.E. Fitzpatrick, A. Lodini, *Analysis of residual stress using neutron and synchrotron radiation* (Taylor & Francis, London, 2003), pp. 10–25
25. S.X. Li, E.G. Ellison, D.J. Smith, *J. Strain Anal.* **29**, 147 (1994)
26. V. Sass, U. Glatzel, M. Feller-Kniepmeier, *Acta Mater.* **44**, 5 (1996)
27. C.G. Dunn, E.F. Koch, *Acta Metall.* **5**, 548 (1957)
28. A.C. Yeh, C.M.F. Rae, S. Tin, *Superalloys* **2004**, 677 (2004)
29. C. Mayr, G. Eggeler, A. Dlouhy, *Mater. Sci. Eng., A* **207**, 51 (1996)
30. D. Mukherji, H. Gabrisch, W. Chen et al., *Acta Mater.* **45**, 3143 (1997)
31. M. Kamaraj, C. Mayr, M. Kolbe et al., *Acta Mater.* **38**, 589 (1998)
32. D. Mukherji, R.P. Wahi, *Scr. Mater.* **36**, 1233 (1997)
33. G.C. Weatherly, *Metal Sci.* **2**, 25 (1968)
34. T.M. Pollock, A.S. Argon, *Acta Metall. Mater.* **40**, 1 (1992)
35. L. Müller, U. Glatzel, M. Feller-Kniepmeier, *Acta Metall. Mater.* **41**, 3401 (1993)